
**SENSITIVITY TO POINT-SPREAD
FUNCTION PARAMETERS IN MEDICAL
ULTRASOUND IMAGE DECONVOLUTION**

H.-C. Shin, R. W. Prager,
J. K. H. Ng, W. H. Gomersall,
N. G. Kingsbury, G. M. Treece and A. H. Gee

CUED / F-INFENG / TR 600

30 April 2008

Department of Engineering
University of Cambridge
Trumpington Street
Cambridge, CB2 1PZ
United Kingdom

Email:

hs338/rwp/jkhn2/whg21/ngk/gmt11/ahg@eng.cam.ac.uk

Sensitivity to Point-Spread Function Parameters in Medical Ultrasound Image Deconvolution

Ho-Chul Shin, Richard Prager, James Ng, Henry Gomersall,
Nick Kingsbury, Graham Treece and Andrew Gee

*Department of Engineering, University of Cambridge,
Trumpington Street, Cambridge, CB2 1PZ, United Kingdom*

Abstract

The resolution of ultrasound images can be improved by deconvolving the images with an estimate of the point-spread function. However, it is difficult to obtain an accurate estimate of the point-spread function *in vivo* because of the unknown properties of the soft tissue through which the signal propagates. The purpose of this paper is to explore the sensitivity of a state-of-the-art deconvolution algorithm to uncertainty in the point-spread function. We present simulated and *in vitro* sensitivity analyses of two-dimensional deconvolution while varying six parameters on which the point-spread function depends. The results are analysed both quantitatively and in terms of the perceived image quality. Our findings indicate that effective deconvolution can be performed without stringent tolerances on the accuracy of the assumed point-spread function. These findings are confirmed in a further experiment involving the deconvolution of an *in vivo* ultrasound image.

PACS: 43.80.Vj; 43.60.Fg; 87.63.dh

Keywords: medical ultrasound image; non-blind deconvolution; image restoration; point-spread function; dual-tree complex wavelet transform

1 Introduction

Ultrasound scanners are widely used in medical imaging applications [1, 2, 3]. Compared to most other modalities, they are safe, portable, quick and cost-effective. Ultrasound scanners do, however, produce images which are often hard to interpret due to the nature of the image formation process. Noticeable effects are blurring in areas of the image which are not well focused, and the presence of a characteristic pattern called speckle, which results from the constructive and destructive interference of scatterers within the range of the point-spread function (PSF) of the ultrasonic imaging system. The larger the main lobe of the PSF, the coarser the speckle.

Deblurring has been a keenly pursued topic in the realm of general image signal processing. It is one of main objectives of image restoration. The physical phenomenon of blurring is mathematically modelled as convolution, hence deblurring can be described as deconvolution. For the

process of deconvolution, two distinct approaches have been developed depending on the availability of prior knowledge of the point-spread function: blind and non-blind deconvolution. Non-blind algorithms are generally more successful than blind techniques as they make use of more prior information. In [4, 5, 6], we proposed an efficient, novel, non-blind deconvolution algorithm which is capable of taking into account the structure of ultrasound speckle. However, the algorithm requires prior knowledge of the PSF. While this can be measured *in vitro* or calculated from knowledge of the transducer design, there is always uncertainty *in vivo* because of variability in the overlying tissue through which any scan must be performed. The main motive of this paper is therefore to establish the sensitivity of the deconvolution algorithm to variation in the assumed PSF, and consequently to establish the feasibility of deconvolution *in vivo*, where the exact PSF is unknown.

2 Non-blind ultrasound deconvolution

2.1 Ultrasound image formulation

The A-lines of an ultrasound imaging system can be mathematically modelled as a Fredholm integral of the first kind [4]. Without loss of generality, if we adopt a *discrete* space-time formulation, the integral can be further simplified using a vector-matrix notation with \mathbf{x} as the field of scatterers and \mathbf{y} as the ultrasound signals:

$$\mathbf{y} = \mathbf{H} \mathbf{x} \quad (1)$$

\mathbf{H} is a block diagonal matrix along the lateral and elevational dimensions. Each block matrix maps from the axial depth dimension to the time domain at a given lateral and elevational position. Here, multi-dimensional images are rearranged into 1D equivalents by lexicographic orders, and hence \mathbf{x} is a $N_x N_y N_z \times 1$ vector, \mathbf{H} is a $N_x N_y N_t \times N_x N_y N_z$ matrix, and \mathbf{y} is a $N_x N_y N_t \times 1$ vector. Although N_t is usually assumed to be equal to N_z , we distinguish them at this stage to highlight the mapping from the spatial z to the temporal t dimension achieved by the operator \mathbf{H} .

It is worth noting that, in traditional deconvolution algorithms, a blurring function is usually assumed to be spatially shift invariant. This tends to be true along the lateral and elevational dimension of an ultrasound image, but the blurring function is significantly shift dependent in the axial direction (i.e. with depth). Our deconvolution algorithm is therefore designed to be capable of dealing with the blurring operator (\mathbf{H}) as spatially shift dependent along the axial direction and shift invariant along the lateral and elevational dimensions [4].

2.2 Deconvolution

Further to the discrete modelling of the Fredholm integral equation, we introduce additive noise (\mathbf{n}) to take into account potential measurement errors [5]:

$$\mathbf{y} = \mathbf{H} \mathbf{x} + \mathbf{n} \quad (2)$$

Our goal is therefore to estimate \mathbf{x} from a noisy and blurred image \mathbf{y} . For simplicity, we denote the sizes of the vectors and the matrix as $N \times 1$ for \mathbf{x} , \mathbf{n} , and \mathbf{y} , and $N \times N$ for \mathbf{H} .

Our deconvolution algorithm operates in a Bayesian context. The scatterer field (\mathbf{x}) is estimated from the observed blurred ultrasound image (\mathbf{y}) corrupted by Gaussian noise (\mathbf{n}). Because of the

ill-posed blurring process (\mathbf{H}), a direct inverse approach is likely to fail, hence regularisation is incorporated in a maximum *a posteriori* framework [7] with a prior on the scatterer field. Possible priors could involve assuming Gaussian or Laplacian statistics for the scatterer field. The Gaussian prior, in particular, leads to the well-known Wiener filter solution, and in a further simplified case, to zero-order Tikhonov regularisation. Instead of using these conventional priors for the entire tissue (\mathbf{x}), a unique feature of our algorithm is the efficient modelling of tissue reflectivity as the product of a macroscopically smooth tissue-type image called the echogenicity map (\mathbf{S}) and microscopically randomised fluctuations (\mathbf{w}) [5]:

$$\mathbf{x} = \mathbf{S} \mathbf{w} . \quad (3)$$

Here, \mathbf{w} is a $N \times 1$ vector, and \mathbf{S} is a $N \times N$ diagonal matrix.

Our algorithm uses wavelet-based denoising to separate \mathbf{x} into its \mathbf{w} and \mathbf{S} components. We therefore represent the reflectivity function (\mathbf{x}) using the dual-tree complex wavelet transform [8, 9] which has been shown to be particularly effective in denoising applications [10]. Finally, we incorporated an Expectation-Maximisation [7] iterative algorithm in which the echogenicity map (\mathbf{S}) is gradually denoised by the wavelet shrinkage rule and the overall scatterer field (\mathbf{x}) is estimated using a Wiener regularisation process by assigning a Gaussian prior to \mathbf{w} .

2.3 Estimation of the PSF

To estimate the PSF, we use Field II simulation program [11, 12]. The transducer parameters studied in this paper are the width of the transducer elements in the lateral direction (width), the width of the transducer elements in the elevational direction (height), the distance between the elements in the lateral direction (kerf), the radius of the elevational focus (Rfocus), the axial depth of the lateral focus (focus), and the system impulse response. The terms inside the brackets refer to the notation in the Field II users' guide.

We convert the pulse-echo response obtained from Field II into its complex baseband counterpart. This enables the data to be downsampled in the axial direction without introducing aliasing. The demodulated data is then low-pass filtered and downsampled to match the size of an image. At this point, we have calculated the matrix \mathbf{H} in our discrete model of the deconvolution problem in Equation (1). Next, the discrete Fourier transform is applied along the lateral and elevational dimensions, because \mathbf{H} is shift invariant in these dimensions and so efficient Fourier domain convolution methods may be used. The pulse-echo data generated in this way is used as a basis for the comparison of different PSFs, which are presented later in the paper.

3 Simulation model

In the previous section, we chose to present key equations in 3D spatial coordinates for completeness. However, in the following simulation work, we use only two-dimensional data, with 2D blurring of the ultrasound images [13]. This is mainly because of limits on computational resources. We wanted to investigate as many variations as possible to reach concrete conclusions, but running a single 3D case is equivalent to running orders of magnitude more 2D cases.

For the simulations described below, we first chose a reference set of input parameters for Field

sampling frequency	66.67 MHz
speed of sound	1540 m/s
number of elements	128
width (of element)	0.1708 mm
height (of element)	6 mm
kerf (gap between elements)	0.025 mm
Rfocus	13 mm
focus	16 mm at depth

Table 1: Reference parameters for simulation.

II. We then created a reflectivity function (\mathbf{x}). Next, we calculated a pulse-echo response PSF, which was shift-invariant in the lateral dimension but shift-dependent in the axial direction, and its kernel was demodulated and downsampled to our format of the PSF (\mathbf{H}). The reflectivity function was then convolved with the PSF and white Gaussian noise was added. Subsequently the same PSF was used for the deconvolution of the simulated, blurred and noisy image.

3.1 Simulation parameters

The reference parameters in Table 1 were chosen to be similar to some ultrasound transducers and acquisition systems that we own. With these parameters, the field of view (FOV) for 2D images is 24.8 mm.

One crucial parameter that is missing from Table 1 is the electro-mechanical impulse response. We estimated this empirically by processing *in vitro* data acquired by one of our ultrasound systems which has a similar configuration to the one in Table 1. A phantom of weak scatterers was scanned and its data was analysed by a linear prediction technique [14] to yield the estimate of the impulse response. See Appendix (A) for further details.

3.2 Simulated reflectivity function

A two-dimensional imaginary phantom was created with five cysts (see Figure 1). The diameter of each cyst is 6.5 mm. Their centres are located at 10 (for two cysts), 16 and 22 mm (for two cysts) away from the probe surface. The bright cysts are ten times stronger than the background scatterers, the dark ones are ten times weaker, and the medium one is three times stronger. This five-cyst image corresponds to an echogenicity map (\mathbf{S}) characterised by macroscopically smooth features. The reflectivity within each scatterer type is then made random by incorporating a Gaussian distribution which represents microscopic fluctuations (\mathbf{w}). A reference image (\mathbf{x}) for the scatterer field is shown in Figure 1(a). After a down-sampling by nine in the axial depth direction, the size in pixels is 256 (in depth) \times 128 (in lateral width).

3.3 Simulated image formation

We blur each scatterer field by calculating a forward convolution of the image in Figure 1(a) with the PSF evaluated by Field II. This convolution approach was chosen over another possible way of blurring using Field II alone because it is faster to run and makes it easier to quantify the effect of the deconvolution later in the work. The time taken for creating the PSF by Field II is significantly lower than that required to blur the entire scatterer field directly by Field II. This is

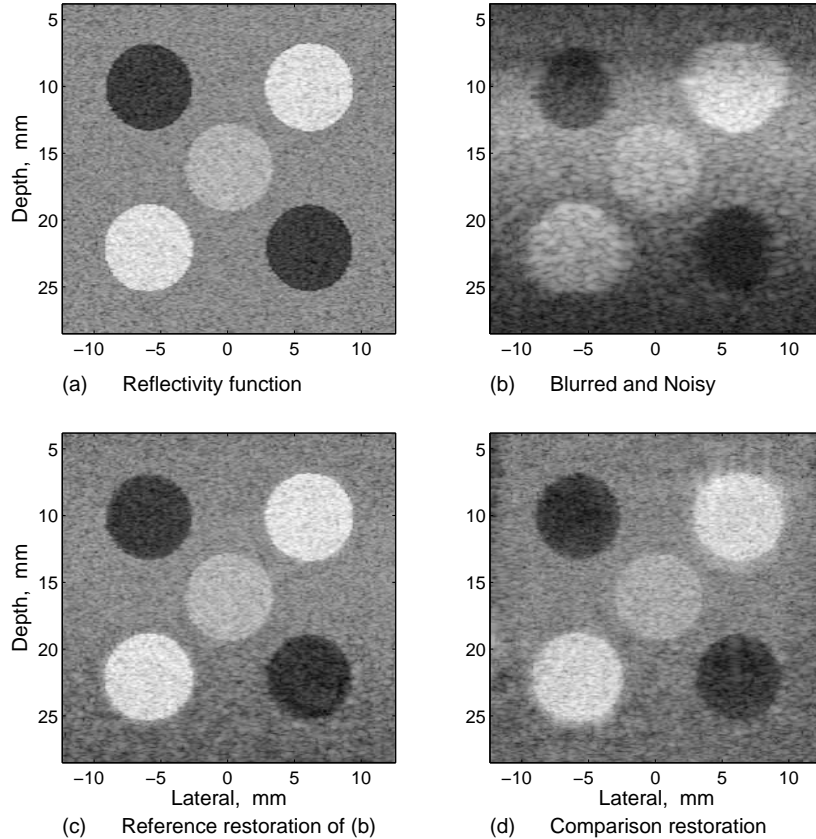


Figure 1: Reference images for the simulation. (a) reflectivity function or scatterer field, (b) blurred image with additive white Gaussian noise of $\text{SNR} = 40$ dB, (c) reference deconvolution of the image in (b), and (d) deconvolution of a noisy image blurred solely by Field II, which is not shown here. The dynamic range of the logarithmically compressed images is 80 dB. The probe surface corresponds to a value of zero in the axial depth dimension.

because for the former we do not need to calculate the PSF for the entire image due to its finite support and it being shift-invariant in the lateral and elevational dimensions, and for the latter approach, to create a realistic ultrasound image, the number of scatterers needs to be much more than the number of pixels.

After blurring, zero-mean white Gaussian noise (\mathbf{n}) is added to the simulated ultrasound image. The blurred and noisy image used as a reference throughout the simulation part of this paper is shown in Figure 1(b). The signal-to-noise ratio after the addition of zero-mean white Gaussian noise is 40 dB. The image is demodulated to baseband, envelope detected and logarithmically compressed into an 80-dB dynamic range.

In Figure 1(b), we can easily identify the symptoms typically associated with ultrasound imaging. When interpreting this image it is useful to note that the axial depth of the lateral focus is 16 mm and corresponds to the designed centre of the cyst in the middle. More serious blurring is easily spotted for scatterers away from the axial depth of the lateral focus. We can also note that the speckle gets coarser compared to that in Figure 1(a).

3.4 Deconvolution of simulated images

The reference blurred and noisy image is restored using the algorithm in [4, 5], whose core structure was briefly outlined in Section 2. The same PSF used for the blurring was used in the deconvolution. The result is shown in Figure 1(c). A considerable degree of restoration is observed. The cysts appear, once again, as circles with sharp boundaries. Furthermore, the speckle size is significantly reduced, but the speckle is retained, which is important as this textural information can be usefully interpreted in clinical applications.

One may ask why the deconvolved result does not look exactly the same as the designed reflectivity function despite the use of the same PSF for both forward and backward operations in the simulation. This is because of the presence of the additive Gaussian noise, and because of the very nature of blurring which involves some loss of high frequency information.

In the last section, it was explained why the convolution approach was taken for forward blurring. However, readers may ask whether such independent convolution produces a realistic ultrasound blurring. Therefore, we constructed an alternative blurred image by direct use of Field II and the addition of Gaussian noise. The subsequent deconvolution is shown in Figure 1(d). Since both deconvolutions exhibit a similar level of restoration, we are satisfied that the aforementioned advantages of the forward convolution approach do not invalidate the parameter sensitivity study.

4 Quantification of deconvolution results

4.1 Linear metrics

The performance of the deconvolution algorithm may be quantified by using the improvement in the signal-to-noise ratio (ISNR, dB). This is defined as [5]

$$\text{ISNR} = 20 \log_{10} \left(\frac{\|\mathbf{y} - \mathbf{x}\|}{\|\hat{\mathbf{x}} - \mathbf{x}\|} \right). \quad (4)$$

where \mathbf{x} is the true scatterer field, as shown in Figure 1(a); \mathbf{y} is the blurred baseband image from the ultrasonic transducer, as shown in Figure 1(b); and $\hat{\mathbf{x}}$ is an estimate of the scatterer field, obtained from the deconvolution process, as shown in Figure 1(c). This approach is straightforward, but applicable only to a simulation, where the true field is known.

Since in this paper the PSFs are deliberately modified by adjusting their parameters, we can also evaluate the discrepancy between them by introducing matrix norms. The ‘PSF match’ is defined as the logarithm of a ratio:

$$\text{PSF match} = 20 \log_{10} \left(\frac{\|\mathbf{H}_r\|_F}{\|\mathbf{H}_v - \mathbf{H}_r\|_F} \right). \quad (5)$$

where $\|\cdot\|_F$ denotes the Frobenius norm of a matrix. The subscript r denotes the *reference* case where the PSF is represented by the set of fixed parameters in Table 1, and v is for cases of numerous *varied* PSFs due to changes in the parameters.

4.2 Logarithmic metric

In the previous section, we discussed metrics based on *linear* values. Here we mean linear in the sense that the arguments of the final logarithm are linear. This is because our restoration model and the related fundamental physics operate on linear values. The ISNR defined in Equation (4) (which we refer to as the *linear* ISNR henceforth) yielded useful values when evaluating the performances of different restoration algorithms [5].

However, in the context of this paper where the aim is to investigate sensitivity within the same deconvolution algorithm, we have discovered that the linear ISNR is not adequate to assess *perceptual* differences between cases with different parameters. The drawback of the linear ISNR is mainly because discrepancies in dark cysts are not weighted as much as those in bright cysts, because the amplitude of dark cysts is usually several orders of magnitude lower. B-scan ultrasound images are always displayed using logarithmic compression. It is on such images that our perceptual evaluation is based. Hence, a modified metric is required to weight the errors in dark cysts as much as those in bright cysts. Therefore, we have replaced linear arguments with logarithmic ones:

$$\text{logarithmic ISNR} = 20 \log_{10} \left(\frac{\| \log |\mathbf{y}| - \log |\mathbf{x}| \|}{\| \log |\hat{\mathbf{x}}| - \log |\mathbf{x}| \|} \right). \quad (6)$$

It should also be noted that we judge images in the magnitude domain since B-scans are displayed after envelope detection. Thus, the logarithmic ISNR based on magnitude information may be more relevant to perceptual evaluation than its linear counterpart in Equation (4), which is calculated in the complex domain.

5 Parameter sensitivity in simulation

Among the various parameters that define the PSF, we will study six to assess their effects on the deconvolution results. These are: the axial depth of the lateral focus (focus), the radius of the elevational focus (Rfocus), the width of the transducer elements in the elevational direction (height), the width of the elements in the lateral direction (width), the speed of sound in soft tissue, and the attenuation rate of the electro-mechanical impulse response.

We chose to change each parameter of the PSF one at a time while the others were fixed at the values in Table 1. Simultaneous variation of two or more parameters would be computationally infeasible. However, the approximately linear nature of the system enables such multivariate situations to be inferred from the cases of single parameter variation. We also assume that the electro-mechanical elements in the transducer aperture are identical and hence we do not investigate the effect of variation in individual elements.

In the following parameter study, the reference blurred image in Figure 1(b) is deconvolved using an assumed PSF with parameters that differ from the reference set. Since the deconvolution is performed using an *incorrect* PSF, we expect the restored image not to be as good as the one in Figure 1(c).

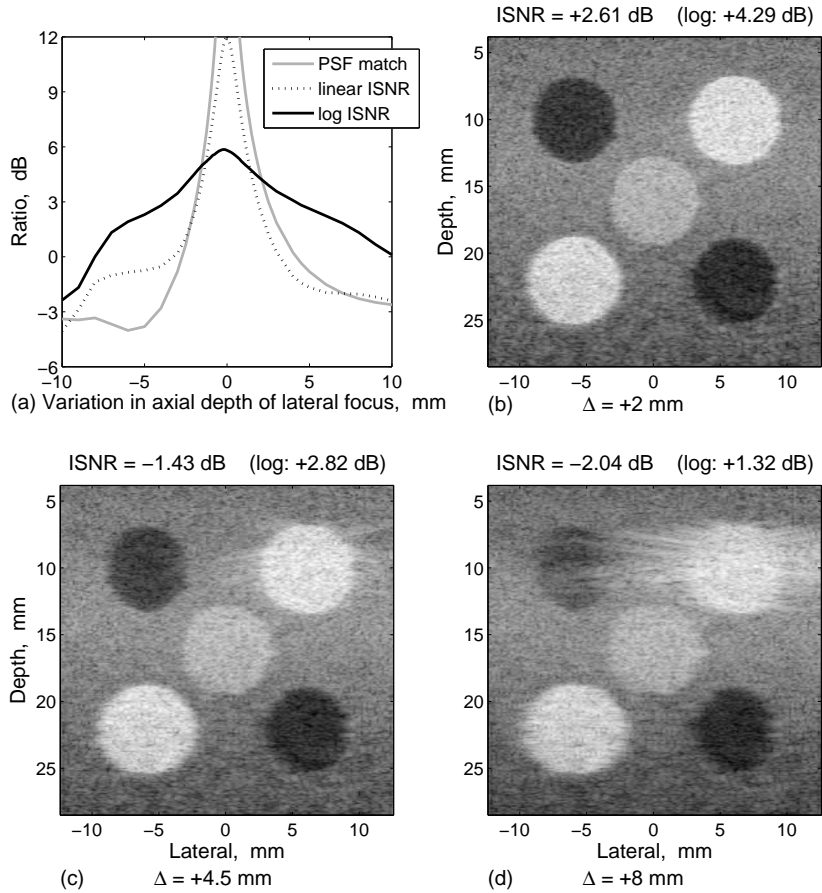


Figure 2: Effect of the variation in the axial depth of the lateral focus: the PSF match vs. ISNR values and examples of deconvolved images. The reference focal depth is 16 mm. The dynamic range of the logarithmically compressed magnitude of the B-scan images is 80 dB. The title of each B-scan image shows two ISNR measures. The left value gives the linear version of the ISNR and the right value inside brackets gives the logarithmic version. The reference values are +12.04 and +5.81 dB respectively. Images are chosen based on their logarithmic ISNR: plot (b) has a logarithmic ISNR of approximately 1.5 dB lower than that of the reference scenario, plot (c) is 3.0 dB lower, and plot (d) is 4.5 dB lower. The same convention is adopted in subsequent figures of simulation.

5.1 Axial depth of the lateral focus

The axial depth of the lateral focus (henceforth, lateral focus for short) is controlled by beamforming delays to each transducer element. It is therefore a readily available quantity when the speed of sound is known. However, it is likely that the focus realised when scanning inhomogeneous tissue will not be the same as that intended, primarily because of speed of sound variation. We investigated deconvolution sensitivity by changing the focus as much as 10 mm away from the reference focus of 16 mm.

We present the simulation results in figures with four subplots. Their format and general notation are explained in the caption to Figure 2. It is easy to see the common qualitative trend between the linear ISNR and the PSF match. There is, however, a qualitative difference between the logarithmic ISNR and the PSF match. Especially for the case of lateral focus variation, we

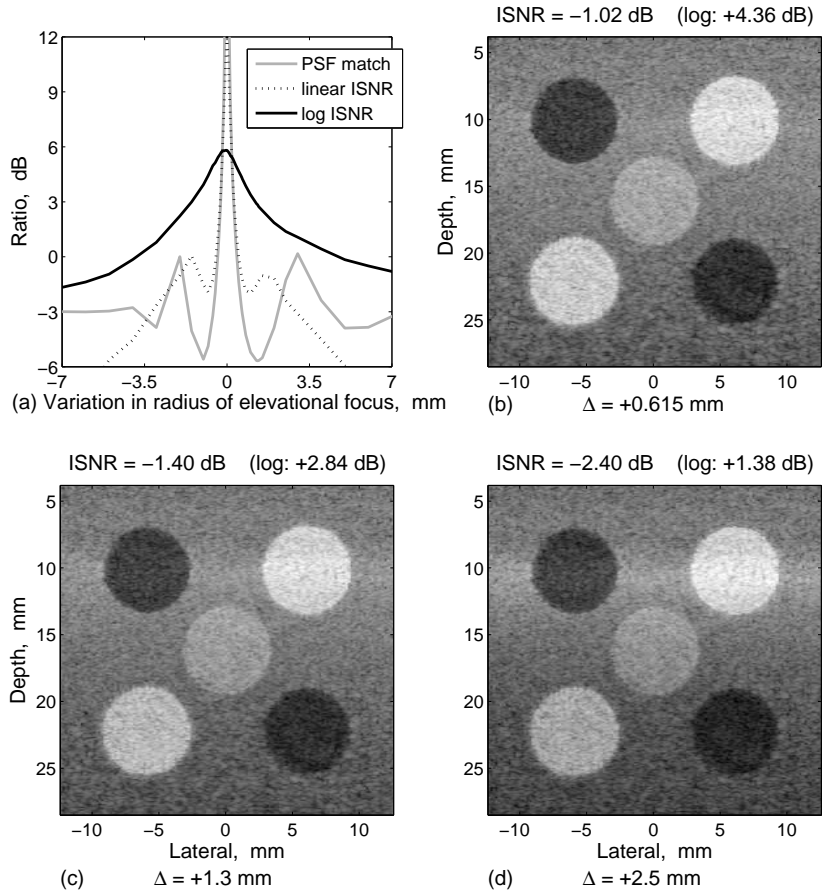


Figure 3: Effect of the variation in the radius of the elevational focus: the PSF match vs. ISNR values and examples of deconvolution images. The reference focal radius is 13 mm.

characterise the logarithmic ISNR as a *single-slope* curve, because its rate of degradation does not experience a significant change in either direction and the curve keeps decreasing.

In addition to the ISNR plot, we can also assess the perceived quality of the deconvolved images,[‡] which are shown in the subplots (b), (c) and (d). When subplot (b) is compared to the solution using the exact PSF in Figure 1(c), there is no significant perceptual difference between the two. In other subplots, we can see the gradual deterioration of the restored images. Considering the two ISNR measures for the sample images, we may conclude that the logarithmic ISNR is better suited than its linear counterpart to describe the human perception of the ultrasound images.

5.2 Radius of the elevational focus

Unlike the lateral focus which is controlled by a beamformer, the radius of the elevational focus (henceforth, referred to as the elevational focus) is fixed at the factory through the design of the acoustic lens. As with the lateral focus, it may not be possible to predict the effective focal length in a practical *in vivo* scan of potentially inhomogeneous soft tissue.

The subplot (a) in Figure 3 shows its sensitivity by means of the deconvolution ISNR and the

[‡]Some subtle differences in perceptual evaluation may not be obvious in the printed version of this paper: readers are encouraged to inspect the images in the electronic format.

PSF match. Again, we observe a close match between the linear ISNR and the PSF match. Both show a fluctuation quite different from the graphs for the lateral focus. The logarithmic ISNR trend is also significantly different: we characterise it as a *dual-slope* curve, since the initial slopes around the peak are much higher than those near the values of ± 7 mm.

Visual inspection of the restored images reveals that subplot (b) is as good as the exact-PSF restoration in Figure 1(c). Since the sample B-scan images have a similar logarithmic ISNR, one might expect the same trend of degradation for subplot counterparts between different parameter variations. This seems to be the case for the subplots (b) between the lateral and elevational foci variation. But a rather different degradation is noticed between subplots (c) and (d). If a priority of perceptual evaluation is put on the sharpness of the restored cyst edges, one may find that the level of restoration in subplots (c) and (d) of the elevational focus is as good as that of the subplot (b).

At this stage, readers may wonder why both ISNR measures show a significant reduction in decibels, although the restored images are noticeably *deblurred*. This may be because there are two main factors that influence the ISNR. One is the level of blurring, the other is the scaling of the solution. Such scaling may be observed between subplot (b) and the others in Figure 3.

We may conclude that there is a systematic difference in the sensitivity to variation of the lateral focus and the elevational focus. When the lateral focus is varied, the changes in the logarithmic ISNR are associated with deblurring. However, the variation in the elevational focus seems to result in changes in image intensity. This can be explained by the fact that the blurring of a *two-dimensional* ultrasound image is created mainly by beamforming in the lateral direction: changing the lateral focus changes the blurring characteristics. However, for the elevational focus, the acoustic lens merely guides the beamformed sound. Therefore, a biased PSF may result in the wrong level of intensity in the restored image.

5.3 Height of the transducer elements

We chose a reference height of 6 mm and changed its value over a range of ± 2 mm. The quantitative measures of the restoration are shown in Figure 4(a), and examples of the deconvolved images are shown in Figure 4(b), (c), and (d). The characteristics of the variation of the elemental height are very similar to those of the elevational focus. The deblurring is effective through a wide range of parameter values but there is evidence of incorrect scaling and the logarithmic ISNR shows a *dual-slope* tendency.

Such similarity may be attributed to the fact that the element height is strongly associated with the dimensions of the acoustic lens in the elevational direction, and hence its variation could affect the performance of the lens, even though the radius of the elevational focus is fixed in this simulation. In addition, the element height does not play a role in the inter-elemental time delays central to lateral focusing.

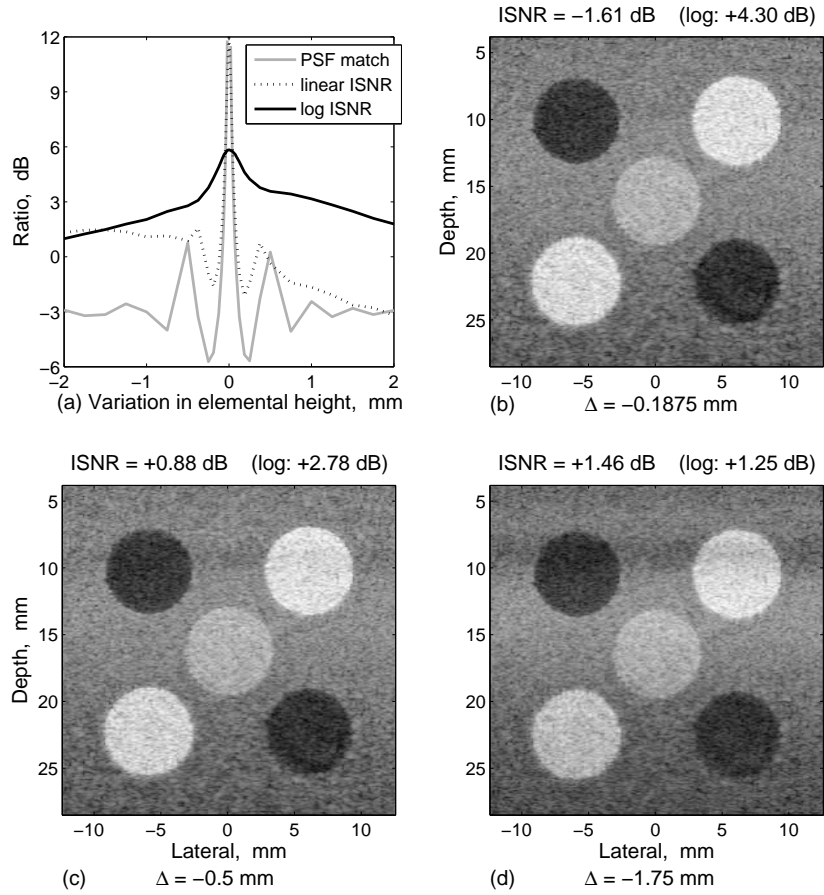


Figure 4: Effect of the variation in the height of the transducer elements: the PSF match vs. ISNR values and examples of deconvolution images. The reference height is 6 mm.

5.4 Width of the transducer elements

For this part of the study, we assume that the FOV and the number of elements are fixed at 24.8 mm and 128 respectively. A reference width of $170.8 \mu\text{m}$ is chosen and varied over the range of $\pm 20 \mu\text{m}$. The kerf is also modified accordingly to maintain a constant spacing between element centres.

We have previously observed that the curves of the PSF match and linear ISNR share a general trend. However, in Figure 5, the linear ISNR appears effectively constant over the range shown in the plot, which covers $\pm 12\%$ of the reference width. While the PSF match shows very acute sensitivity, its decibel value is much higher than for the variation of the other parameters, implying that these PSFs are effectively the same as the reference one. Therefore, the element width is not a critical parameter in the deconvolution process. This outcome suggests that the elements and possible uncertainties are small enough in the lateral direction, and hence there is no significant *finite* effect in the width. Figure 5 also indicates that the restored images are not sensitive to variation of the element width, and hence such results are not shown here.

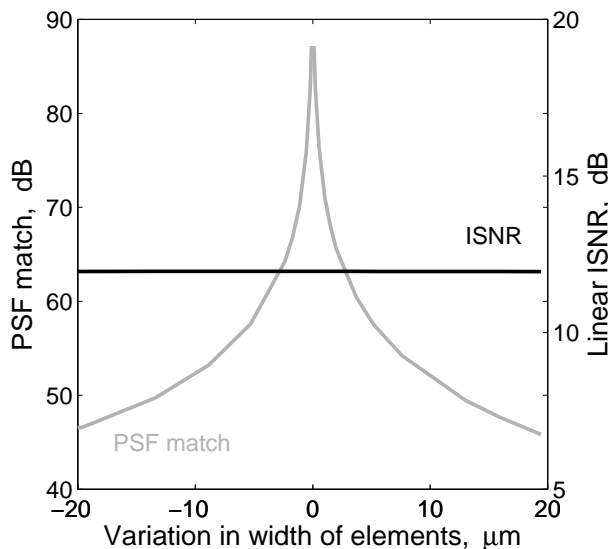


Figure 5: Effect of the variation in the width of the transducer elements on the PSF match and linear ISNR while the field-of-view and number of elements are fixed. The reference width is $170.8 \mu\text{m}$. The decibel values for the PSF match are shown on the left-hand side, and the linear version of the ISNR is shown on the right. The logarithmic version of the ISNR is not shown.

5.5 Speed of sound

So far, we have investigated the sensitivity of parameters specific to ultrasound transducers. Perhaps more uncertainty may reside in parameters found in the tissue than in the transducer. We have therefore included variation in the speed of sound in our sensitivity study.

There is considerable uncertainty in the speed of sound when scanning *in vivo*, both in terms of the absolute speed and its homogeneity. In this section, however, we investigate the sensitivity only under the assumption of an homogeneous medium. In other words, the speed of sound is varied uniformly throughout the tissue away from the nominal 1540 m/s . It is changed over the range of $\pm 200 \text{ m/s}$.

The results in Figure 6 are similar to those for the lateral focus in Figure 2. The logarithmic ISNR can be characterised as a *single-slope* curve and its effect on the B-scan images is one of blurring, not intensity change. Even though the lateral focus of the ultrasound system is fixed, the variation in the speed of sound will change the effective time delays between transducer elements, leading to different blurring characteristics.

5.6 Attenuation in the electro-mechanical impulse response

Another tissue specific parameter is the frequency-dependent attenuation of the ultrasonic signal. Here, we deal with such attenuation by adjusting the frequency spectrum of the electro-mechanical impulse response (henceforth, short as ‘pulse’).

In a real soft tissue environment, frequency-dependent attenuation occurs progressively with propagation distance. However, we simplify the situation by applying frequency-dependent attenuation uniformly throughout the medium. The reference pulse was acquired in a phantom where it could have suffered attenuation of approximately 1.5 dB/MHz . Hence, the attenuation rate was

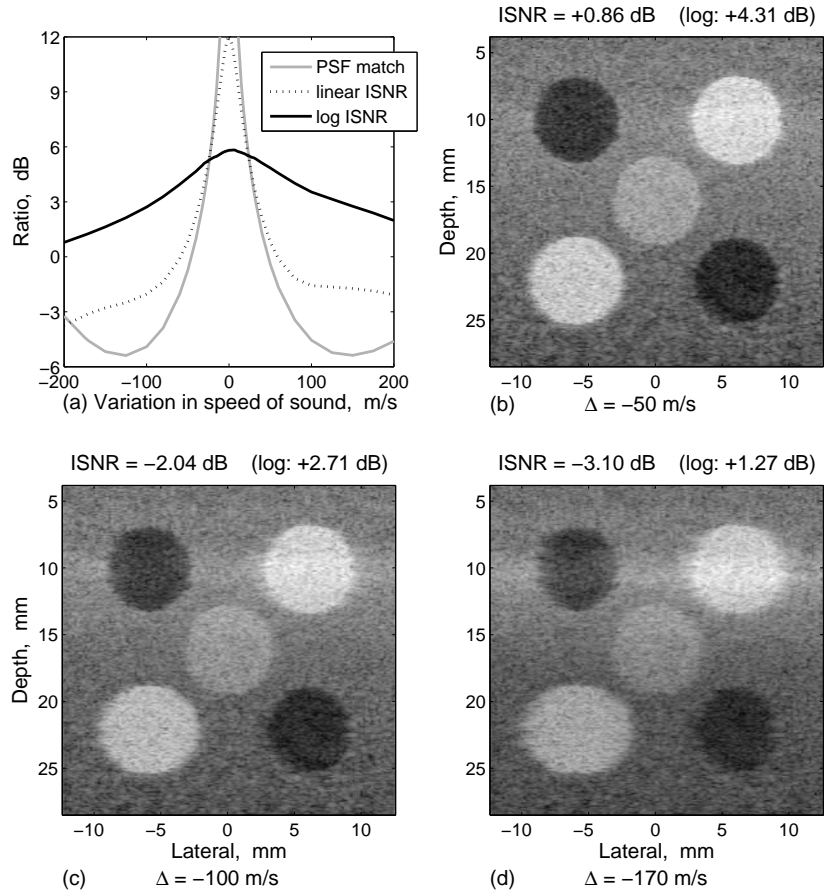


Figure 6: Effect of the uniform variation in the speed of sound in soft tissue: the PSF match vs. ISNR values and examples of deconvolved images. The reference speed is 1540 m/s.

varied from amplification of 1.5 dB/MHz (a hypothetically unattenuated signal) to the extreme case of -10 dB/MHz.

Figure 7 shows the simulation results. In terms of perceptual evaluation, it appears that the deblurring is not especially sensitive to the rate of attenuation. In terms of its operating mechanism, the attenuation rate is not closely related to either beamforming or the acoustic lens aspect of the ultrasound system. Therefore, it is considered to behave independently of any other parameters investigated in this paper.

6 Deconvolution of *in vitro* ultrasound images

It would appear that human perception does not demand exceptionally high accuracy from a deconvolution algorithm. In the previous simulation experiments, we observed negligible change in the perceived image quality as long as the logarithmic ISNR was within -1.5 dB of the ideal solution. In some situations, a reduction in ISNR of as much as 4.5 dB was acceptable, with corresponding PSF parameters significantly beyond the nominal uncertainty in their accuracy.

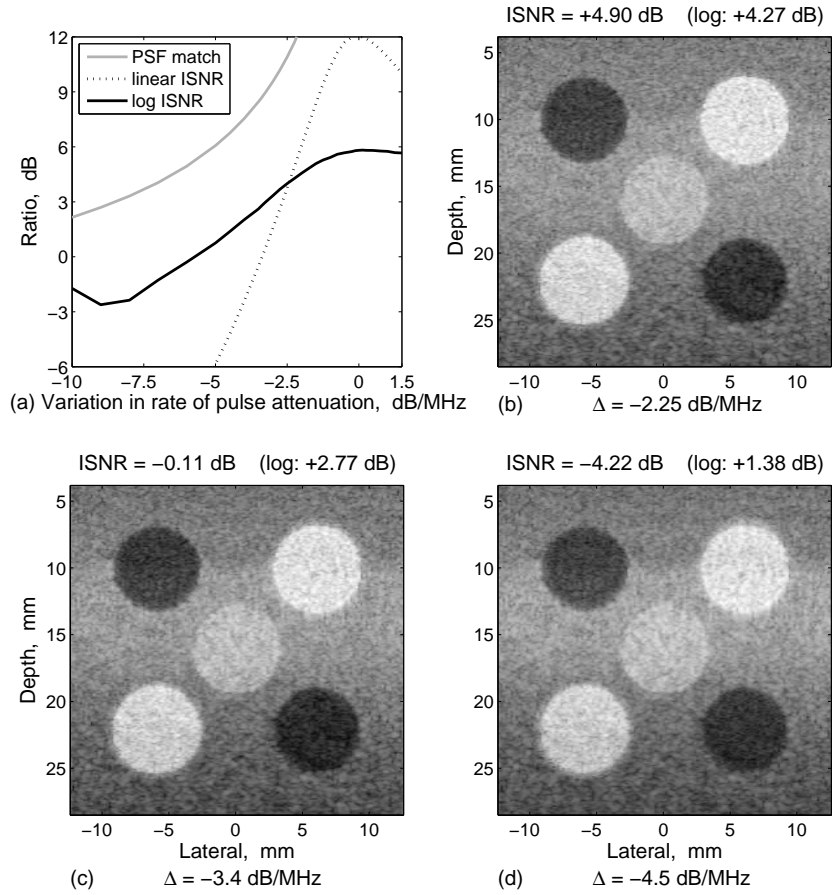


Figure 7: Effect of the uniform variation in the frequency-dependent attenuation of the electro-mechanical impulse response in the ultrasound system: the PSF match vs. ISNR values and examples of deconvolved images.

In this section, we explore whether our assessment from the simulations is observed in more realistic ultrasound images. A custom-made phantom containing several cysts was scanned using a clinical ultrasound system. We assumed the same set of reference parameters as those given in Table 1, apart from the elevational focus and elemental height, whose values are now 9.6 and 3.5 mm respectively. These parameters were chosen to match our best understanding of the transducer geometry.

Even if these parameters were exactly correct, there is another reason why the PSF used for deconvolution may not match the actual PSF *in vitro*. In simulation, we can create an ultrasound image by way of a perfect *two-dimensional* interaction, but in practice ultrasound image formation is a *three-dimensional* process, due to the extension of the resolution cell in the elevational direction. Therefore, the reference *two-dimensional* PSF may not exactly match the ultrasound system's true PSF.

Figure 8 shows the ultrasound image acquired *in vitro* and its restored image using the reference PSF. The deblurring is evident and the cysts recover their circular shape with sharper boundaries. The physical size of the speckle is notably reduced as well.

The amount of deconvolution can be assessed quantitatively by investigating the level of correla-

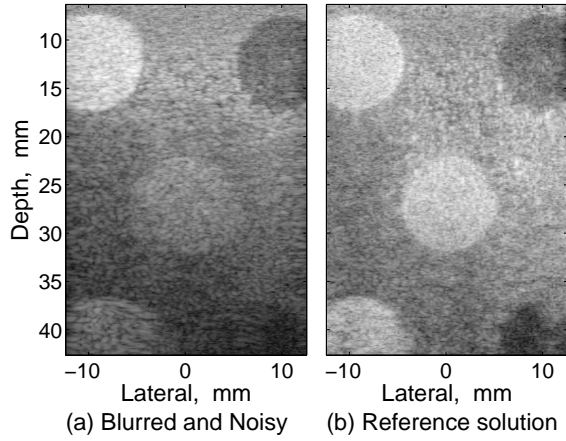


Figure 8: Reference images for *in vitro* phantom. (a) image acquired by an ultrasound machine, (b) deconvolved image using the PSF with the reference parameters. The dynamic range of the logarithmically compressed magnitude of both images is 80 dB.

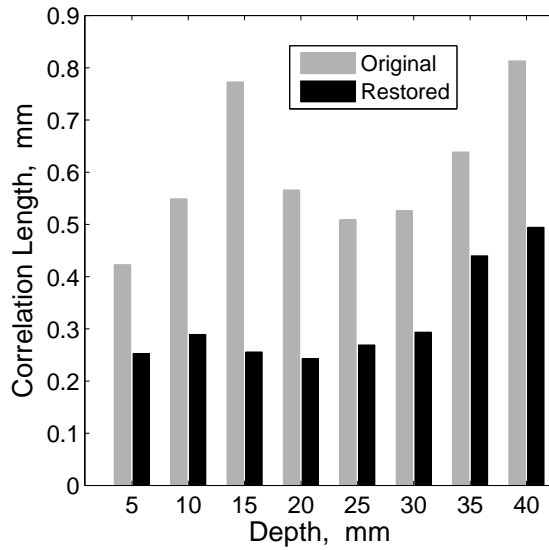


Figure 9: Correlation length in the lateral direction of *in vitro* ultrasound images of a phantom in Figure 8.

tion in ultrasound images. Since the PSF of a typical ultrasound system is spread mainly laterally rather than axially, the effect of deblurring can be gauged by measuring the lateral correlation length at each axial depth. To this effect, the autocorrelation was evaluated and the half-energy width from its peak was recorded. Figure 9 shows a significant reduction in the correlation length for the restored image of Figure 8(b) compared with that of the original image of Figure 8(a). The mean correlation length is 0.61 and 0.32 mm, for the original and the restored image respectively.

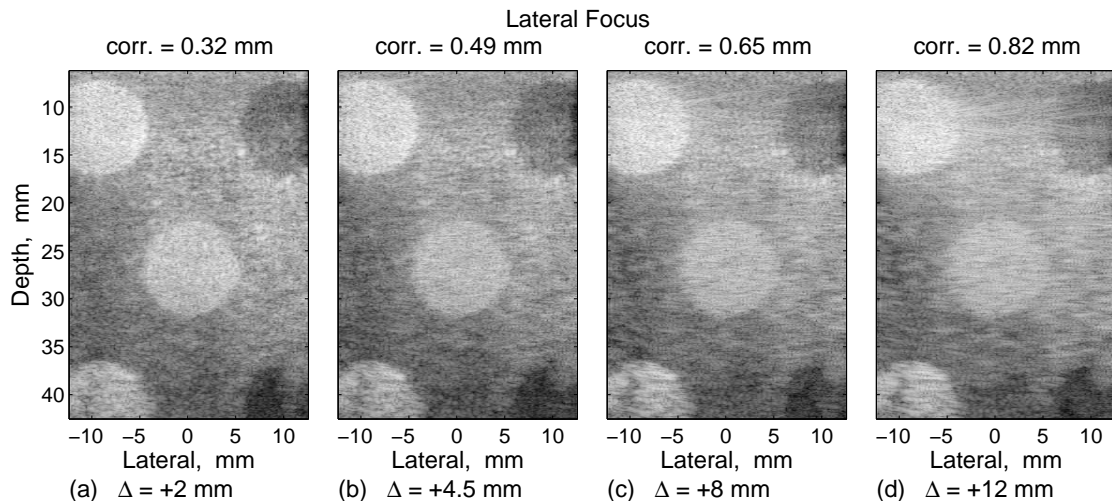


Figure 10: Examples of deconvolved images and their mean correlation length for the *in vitro* phantom with the variation in the axial depth of the lateral focus. The reference focal depth is 16 mm. The dynamic range of the logarithmically compressed magnitude of the images is 80 dB. The title of each image shows its mean correlation length in the lateral direction, and those of the original ultrasound image and the reference deconvolution are 0.61 and 0.32 mm, respectively.

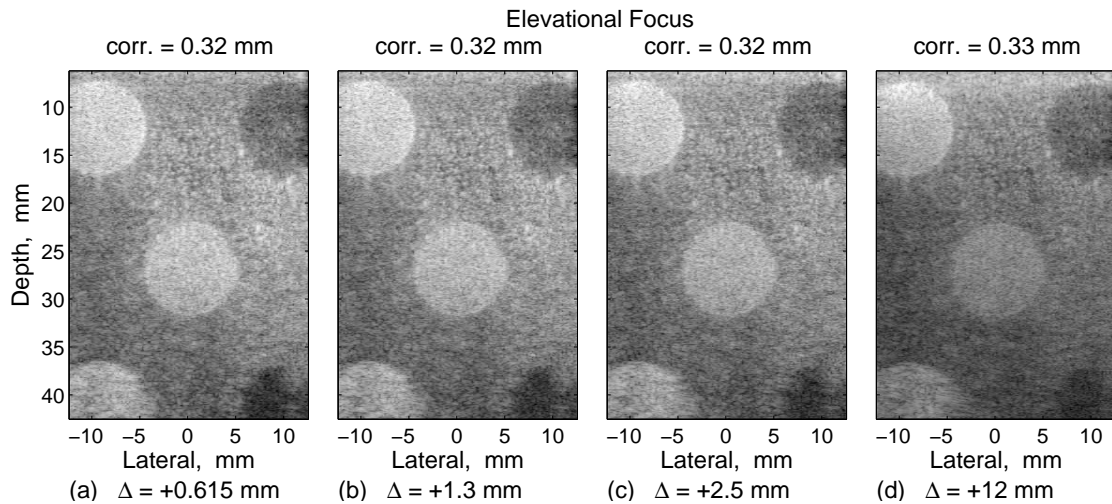


Figure 11: Examples of deconvolved images and their mean correlation length for the *in vitro* phantom with varying values of the radius of the elevational focus. The reference focal radius is 9.6 mm.

Figure 10 shows the restored images when the assumed lateral focus is varied. The errors in the parameter are the same as in the simulations, apart from in the last subplot (d), which shows the effect of a large offset from the correct value. This same convention is followed in subsequent cases. Since we do not know the scatterer field *a priori* for the *in vitro* restorations, the ISNR cannot be evaluated in these cases. However, we provide the mean correlation length in the lateral direction as an alternative way of quantifying the deblurring effect. Perceptually, the *in vitro* study shows a similar trend to that observed in the simulations. Subplot (a) looks very similar to the reference

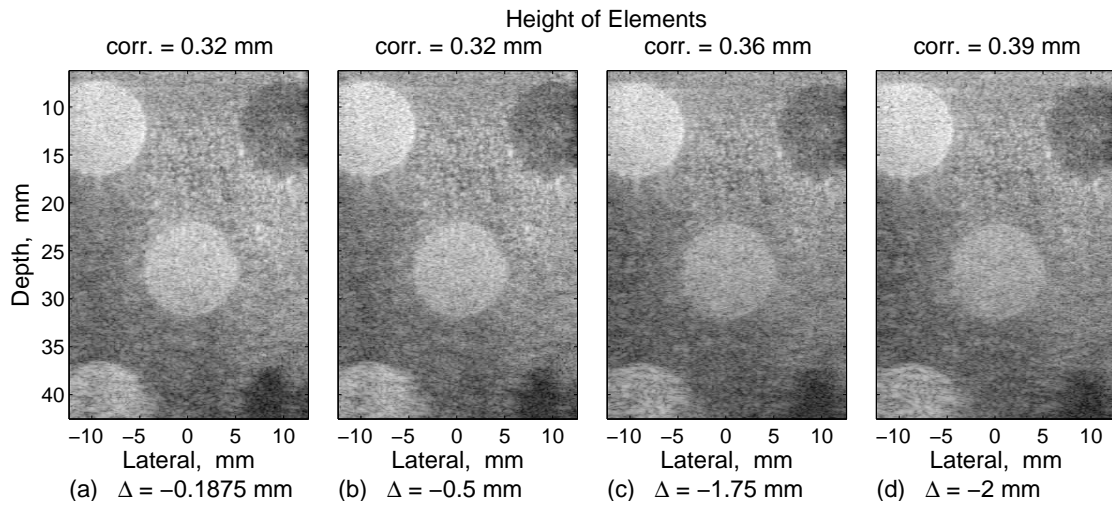


Figure 12: Examples of deconvolved images and their mean correlation length for the *in vitro* phantom for various values of the height of the transducer elements. The reference height is 3.5 mm.

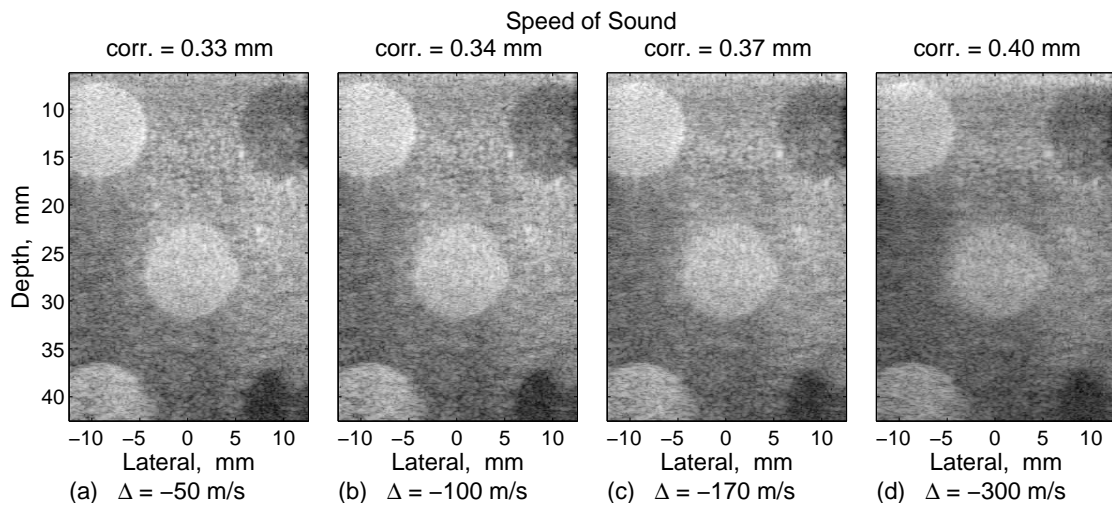


Figure 13: Examples of deconvolved images and their mean correlation length for the *in vitro* phantom for various values of the speed of sound in soft tissue. The reference speed is 1540 m/s.

deconvolution in Figure 8(b), with a gradual reduction in the deblurring capability thereafter.

Figure 11 shows the deconvolution results when the assumed elevational focus is adjusted. In the simulation, we saw that the deterioration of the logarithmic ISNR was related to scaling ambiguity rather than deblurring performance. The same trend is observed in the *in vitro* deconvolution. It is also noted that the correlation length is virtually unchanged. These confirm that deblurring of a *two-dimensional* ultrasound image is mostly unaffected by the assumed elevational focus.

Figure 12 presents the restored images with various values of assumed element height. As with the simulations, the deblurring power is largely unaffected, but there is a subtle difference in the intensity of the restored images.

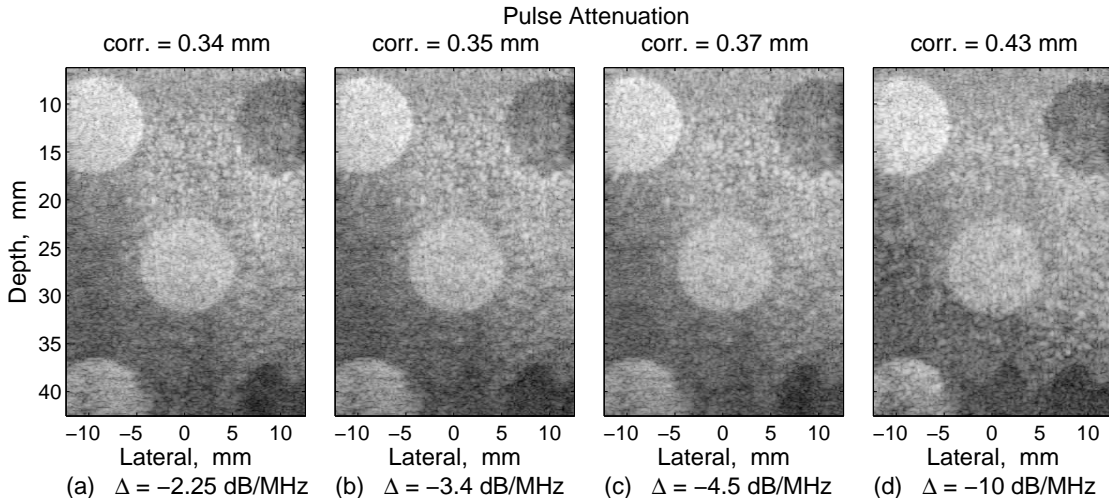


Figure 14: Examples of deconvolved images and their mean correlation length for the *in vitro* phantom assuming various degrees of frequency-dependent attenuation in the electro-mechanical impulse response.

As demonstrated in the simulations, variation in the assumed element width does not produce any noticeable difference when the FOV and the number of elements are fixed. The situation will not be any different *in vitro*, since the PSFs are almost identical.

Figure 13 demonstrates *in vitro* deconvolution using various values for the assumed speed of sound in the phantom. The deterioration in image quality is subtle, but its characteristic seems to be similar to that of the lateral focus. It also appears that the errors in the PSF mainly degrade the deblurring performance of the restoration.

Figure 14 shows the *in vitro* deconvolution when various degrees of frequency-dependent attenuation are assumed in the impulse response of the ultrasound system. The behaviour of this parameter is different from the others. The extreme case of -10 dB/MHz does not show severe lack of deblurring or different background intensity compared with the other values.

These *in vitro* results have confirmed the findings of the simulations. Since the success of deconvolution is perceived primarily in terms of deblurring and not image intensity, the most critical parameters for *two-dimensional* deconvolution are the lateral focus and the speed of sound.

7 Deconvolution of *in vivo* ultrasound image

In this section, we apply our deconvolution algorithm *in vivo*. A clinical ultrasound system was used to scan a left forearm, near the elbow. Figure 15 shows the acquired ultrasound image and its restored version using the PSF used for the reference deconvolution of *in vitro* images.

We expect the discrepancy between reference and true parameters to get even worse *in vivo*, the most significant reason being the inhomogeneous composition of soft tissue. Nonetheless, the deconvolution result illustrates the robustness of our restoration method and its applicability *in vivo*. The physical size of the speckle is reduced and deblurring is evident, especially in the dominant curved feature.

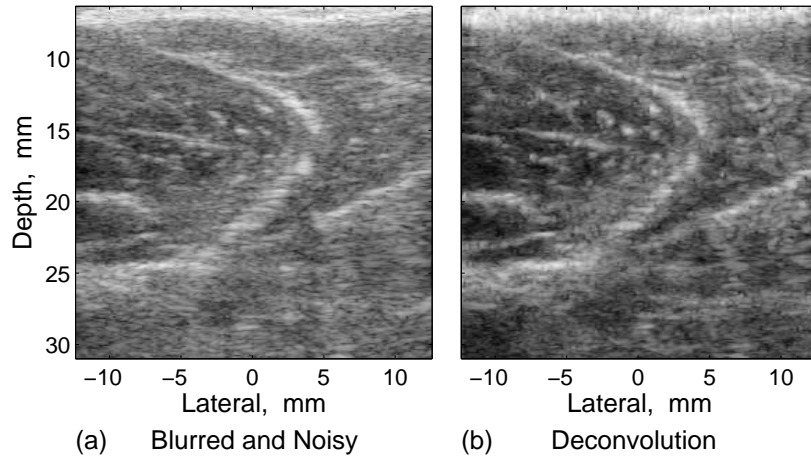


Figure 15: Ultrasound images for *in vivo* forearm. (a) image acquired by an ultrasound machine, (b) restored image using the PSF with the reference parameters. The dynamic range of the logarithmically compressed magnitude of the images is 80 dB.

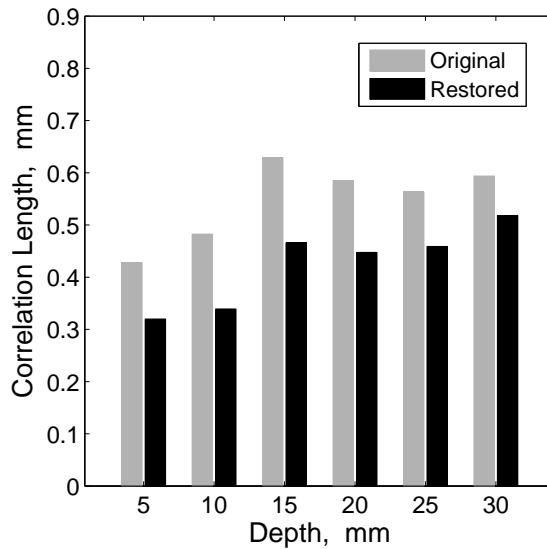


Figure 16: Correlation length in the lateral direction of *in vivo* ultrasound images of a forearm in Figure 15.

The lateral correlation lengths for the *in vivo* images are shown in Figure 16. The reduction is consistent at all depths, though not as significant as the *in vitro* case: this is unsurprising given the likely discrepancy between the assumed and the actual PSF *in vivo*. The mean correlation length is 0.55 mm in the original image and 0.42 mm in the restored image.

8 Conclusions

In the simulations, we observed that the quantitative difference in deconvolution in terms of the *linear* version of the ISNR was similar to that derived from measuring changes directly in the PSF. We believe that the ISNR measure based on the *logarithmic* image amplitude is a better indicator of the perceived improvement in the restored ultrasound images.

Simulation and *in-vitro* studies showed that, in terms of effective deblurring in a *two-dimensional* restoration, the two most influential parameters are the axial depth of the lateral focus and the speed of sound in soft tissue. The other parameters principally adjust the intensity level of the restored image, but do not make significant differences to deblurring.

Based on these perceptual judgements, assisted by the logarithmic ISNR metric, we conclude that a PSF with acceptable accuracy can be estimated in most cases. Satisfactory *in-vivo* deconvolution can normally be accomplished despite imperfect assumptions about the ultrasound system and the soft tissue under examination.

9 Acknowledgements

The work was funded by the Engineering and Physical Sciences Research Council (reference EP/E007112/1) in the United Kingdom.

A Estimation of electro-mechanical impulse response

In this appendix, we briefly describe how the electro-mechanical impulse response (henceforth, referred to as the ‘pulse’) may be estimated using a parametric method based on acquired backscattered RF data.

The use of parametric methods to estimate the shape of the ultrasound pulse was proposed by Jensen [15]. His method assumes an ARMA (auto-regressive moving average) model and the parameters are estimated using acquired A-line data by an iterative gradient-search scheme. Here, however, we discuss the task of estimating the same pulse more simply by using an AR (auto-regressive) model. It is well known that an ARMA model can be approximated by an AR model of sufficiently high order, and AR models may be preferred because their parameters are much easier to estimate.

Parametric methods assume that the observed trace may be represented as the result of filtering a white noise process. If the white noise process is considered to be a random spike series, then this assumption is equivalent to saying that the observed trace is obtained by convolving the underlying pulse onto this spike series [16]. For a region characterised by uniform weak scattering, this appears to be a reasonable assumption to make since the scatterers within the region behave approximately like spikes, randomly spaced and with random scattering strengths.

AR modelling represents the underlying pulse as an all-pole filter. Let the digitised samples of an observed trace be $g(n)$, the white noise process be $e(n)$ and the digitised samples of the pulse be $v(n)$. The corresponding z -transforms are denoted by $G(z)$, $E(z)$, and $V(z)$, respectively. The

filtering operation may be expressed as,

$$G(z) = E(z)V(z) \implies \frac{G(z)}{E(z)} = V(z) = \frac{1}{1 + \sum_{m=1}^M a_m z^{-m}} \quad (7)$$

where a_m is the sequence of filter coefficients that need to be determined to obtain $v(n)$, and M is the order of the AR process. This z -domain equation may also be expressed in the more familiar form of a difference equation:

$$g(n) + \sum_{m=1}^M a_m g(n-m) = e(n) \quad (8)$$

The sequence a_m may be estimated by minimising the error in the least squares sense, for example using the Yule-Walker or normal equation. This procedure is also known in the domain of predictive deconvolution [16] or forward linear prediction [14].

To recover the underlying pulse $v(n)$, the discrete-time Fourier transform $V(e^{j\omega})$ of $v[n]$ can be computed from Equation (7) with the substitution $z = e^{j\omega}$. The inverse Fourier transform is then applied to $V(e^{j\omega})$. We then assumed a minimum phase for the pulse shape. Figure 17 shows an example of an electro-mechanical impulse response estimated by the method outlined here. It is used throughout this paper and acted as the reference pulse when frequency-dependent attenuation was applied.

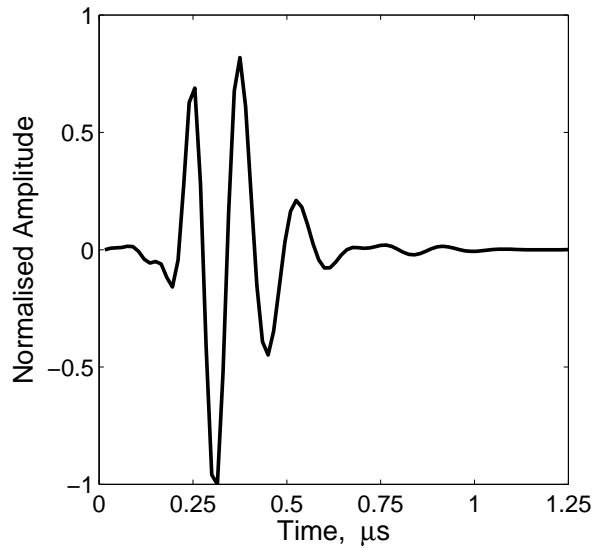


Figure 17: Example of an electro-mechanical impulse response

References

- [1] Z.-H. Cho, J. P. Jones, M. Singh, Foundations of Medical Imaging, John Wiley & Sons, Inc, New York, 1993.

- [2] P. Suetens, *Fundamentals of Medical Imaging*, Cambridge University Press, Cambridge, UK, 2002.
- [3] T. L. Szabo, *Diagnostic Ultrasound Imaging: Inside Out*, Elsevier Academic Press, Amsterdam, 2004.
- [4] J. Ng, R. Prager, N. Kingsbury, G. Treece, A. Gee, Modelling ultrasound imaging as a linear shift-variant system, *IEEE Transactions on Ultrasonics, Ferroelectrics, and Frequency Control* 53 (3) (2006) 549–563.
- [5] J. Ng, R. Prager, N. Kingsbury, G. Treece, A. Gee, Wavelet restoration of medical pulse-echo ultrasound images in an EM framework, *IEEE Transactions on Ultrasonics, Ferroelectrics, and Frequency Control* 54 (3) (2007) 550–568.
- [6] J. Ng, H. Gomersall, R. Prager, N. Kingsbury, G. Treece, A. Gee, Wavelet restoration of three-dimensional medical pulse-echo ultrasound datasets in an EM framework, *Proceedings of the 29th International Symposium on Acoustical Imaging*, Shonan, Kanagawa, Japan, 2007.
- [7] C. W. Therrien, *Discrete Random Signals and Statistical Signal Processing*, Prentice Hall, Inc, Englewood Cliffs, NJ, USA, 1992.
- [8] N. Kingsbury, Image processing with complex wavelets, *Philosophical Transactions of The Royal Society of London Series A* 357 (1999) 2543–2560.
- [9] N. Kingsbury, Complex wavelets for shift invariant analysis and filtering of signals, *Applied and Computational Harmonic Analysis* 10 (2001) 234–253.
- [10] L. Sendur, I. W. Selesnick, Bivariate shrinkage functions for wavelet-based denoising exploiting interscale dependency, *IEEE Transactions on Signal Processing* 50 (11) (2002) 2744–2756.
- [11] J. Jensen, N. B. Svendsen, Calculation of pressure fields from arbitrarily shaped, apodized, and excited ultrasound transducers, *IEEE Transactions on Ultrasonics, Ferroelectrics, and Frequency Control* 39 (1992) 262–267.
- [12] J. Jensen, Field: A program for simulating ultrasound systems, *Medical & Biological Engineering & Computing* 34 (1996) 351–353, presented at the 10th Nordic-Baltic Conference on Biomedical Imaging.
- [13] J. C. Bamber, R. J. Dickinson, Ultrasonic B-scanning: A computer simulation, *Physics in Medicine and Biology* 25 (3) (1980) 463–479.
- [14] J. G. Proakis, G. M. Dimitris, *Digital Signal Processing: Principles, Algorithms, and Application*, Prentice-Hall, London, 1996.
- [15] J. A. Jensen, Estimation of pulses in ultrasound B-scan images, *IEEE transactions on medical imaging* 10 (2) (1991) 164–172.
- [16] E. A. Robinson, S. Treitel, *Applications of Digital Signal Processing*, Prentice-Hall Signal Processing Series, Prentice-Hall, 1978, Ch. Digital Signal Processing in Geophysics.